J. Fluid Mech. (2002), *vol.* 464, *pp.* 345–363.
DOI: 10.1017/S0022112002008923 Printed in the United Kingdom

Low-Prandtl-number convection in a rotating cylindrical annulus

By E. PLAUT[1] AND F. H. BUSSE[2]

[1]LEMTA, INPL-UHP-CNRS, 2 av. de la Fort de Haye, F-54504 Vandoeuvre cedex, France
[2]Institute of Physics, University of Bayreuth, D-95440 Bayreuth, Germany

(Received 18 April 2001 and in revised form 15 February 2002)

Motivated by recent experimental results obtained in a low-Prandtl-number fluid (Jaletzky 1999), we study theoretically the rotating cylindrical annulus model with rigid boundary conditions. A boundary layer theory is presented which allows a systematic study of the linear properties of the system in the asymptotic regime of very fast rotation rates. It shows that the Stewartson layers have a (de)stabilizing influence at (high) low Prandtl numbers. In the weakly nonlinear regime and for low Prandtl numbers, a strong retrograde mean flow develops at quadratic order. The Poiseuille part of this mean flow is determined by an equation obtained by averaging of the Navier–Stokes equation. It thus gives rise to a new global-coupling term in the envelope equation describing modulated waves, which can be used for other systems. The influence of this global-coupling term on the sideband instabilities of the waves is studied. In the strongly nonlinear regime, the waves restabilize against these instabilities at small rotation rates, but they are destabilized by a short-wavelength mode at larger rotation rates. We also find an inversion in the dependence of the amplitude on the Rayleigh number at low Prandtl numbers and intermediate rotation rates.

1. Introduction

The problem of convection driven by radial buoyancy in a rotating cylindrical annulus incorporates some basic physical features of the more complex problem of convection in self-gravitating rotating fluid spheres which is of fundamental importance in theories of planetary interiors and of stars. In fact, it can be shown that the simplest realistic model of the onset of convection in such systems (Busse 1970) is mathematically identical to the problem of convection in a rotating cylindrical annulus with inclined end boundaries (figure 1). In both cases the onset occurs in the form of thermal Rossby waves which propagate in the prograde direction. From this similarity of the two problems at onset, it can be expected that an analogy will persist in the nonlinear regime; this has for instance been used to investigate the generation of strong zonal flows in celestial bodies (Brummell & Hart 1993). The rotating cylindrical annulus model is also of interest as a basic fluid dynamical system, that can be studied in the laboratory. In the experimental realizations (see e.g. Azouni, Bolton & Busse 1986) the centrifugal force assumes the role of gravity. The annular fluid layer thus becomes unstable when the outer cylinder is kept at a temperature T_2 sufficiently higher than the temperature T_1 of the inner cylinder. While the direction of the force is opposite to that realized in self-gravitating spheres, the buoyancy-driven motions occur in the same way as in the case when force and temperature gradient are reversed.

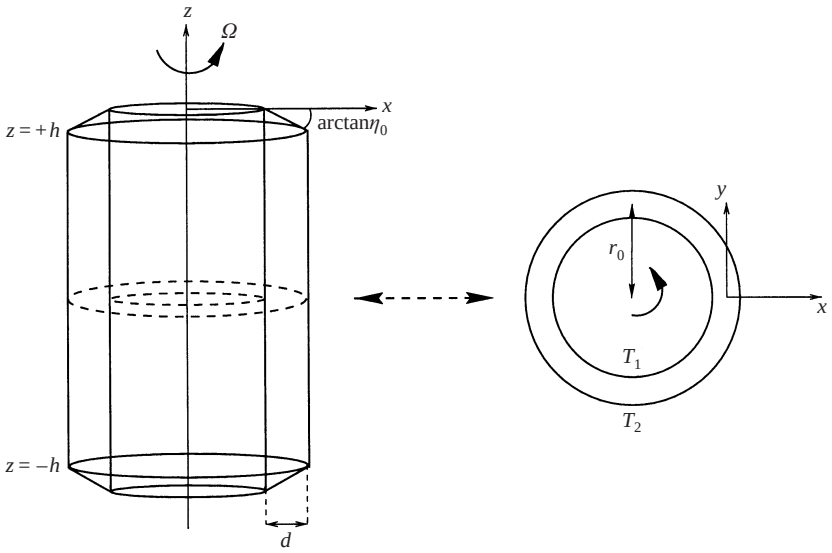

FIGURE 1. The rotating cylindrical annulus geometry.

Besides the Rayleigh number R and the Coriolis parameter η, which are dimensionless measures of the temperature difference between inner and outer cylinder and of the rotation rate Ω, respectively, the Prandtl number P, the ratio between kinematic viscosity ν and thermal diffusivity κ, is an important parameter. In planetary and stellar applications, it takes values much smaller than unity. For this reason experimental (Azouni *et al.* 1986; Jaletzky 1999) as well as theoretical studies (Herrmann & Busse 1997, hereinafter referred to as HB97) have focused on the case of small Prandtl number. For reasons of mathematical simplicity, stress-free or slip conditions at the cylindrical walls have been assumed in most theoretical studies. As a consequence singular behaviour in the limit $P \to 0$ is found, and modulated or chaotic states have been predicted (HB97). These were not seen, however, in the recent experiments by Jaletzky (1999). For this reason a detailed theoretical study of the rotating cylindrical annulus model with realistic no-slip boundary conditions has been undertaken, which is presented in this paper.

After the formulation of the model in § 2, its linear properties are studied in § 3. An analytical theory is derived to approximate the linear no-slip solutions in the limit of large η, and the corresponding Stewartson layers are analysed. In § 4 the weakly nonlinear dynamics is described on the basis of a new envelope equation (4.20). In particular, the global-coupling role of a Poiseuille mean flow generated at quadratic order in the no-slip case is emphasized. Finally, in § 5 a Galerkin method is used to obtain numerical results for the fully nonlinear no-slip problem.

2. The rotating cylindrical annulus model

For a detailed presentation of the rotating cylindrical annulus model we refer the reader to Busse & Or (1986, hereinafter referred to as BO86). The geometry of the problem is defined in figure 1. The gap d between inner and outer cylinder is used as length scale, d^2/ν as time scale, $P(T_2 - T_1)$ as temperature scale. The Rayleigh number R and the Coriolis parameter η are

$$R = \gamma g d^3 (T_2 - T_1)/(\kappa\nu) \quad \text{and} \quad \eta = 2\Omega\eta_0 d^3/(h\nu),$$

with γ the coefficient of thermal expansion, $g = \Omega^2 r_0$ the centrifugal acceleration at the mean radius r_0 of the annular region, and η_0 the slope of the conical caps. Note that η is proportional to the inverse of the Ekman number $E = \nu/(d^2\Omega)$. Because of the small-gap approximation $d \ll r_0$, curvature effects can be neglected and a Cartesian coordinate system x, y, z can be introduced. The annulus is thus unfolded to the domain $\{x \in [-1/2, 1/2], y \in [-L/2, L/2], z \in [-h/d, h/d]\}$ with $L = 2\pi r_0/d \gg 1$. Accordingly periodic boundary conditions are to be used in the y-direction. The Boussinesq approximation is assumed. Because of the assumption $\eta_0 \ll 1$ and of the Proudman–Taylor constraint, the velocity field is z-independent in the lowest approximation,

$$\boldsymbol{v} = (\partial_y \psi)\hat{\boldsymbol{x}} - (\partial_x \psi)\hat{\boldsymbol{y}}, \tag{2.1}$$

with the streamfunction $\psi(x, y, t)$. Integration over z of the equation for the z-component of the vorticity, $\zeta = -\Delta_2 \psi$, and elimination of the z-component of the velocity through the use of the boundary conditions at the conical caps yields an equation for ζ. Together with the heat equation for the deviation $\theta(x, y, t)$ of the temperature from the basic profile of pure conduction, we obtain

$$\partial_t \zeta + \boldsymbol{v} \cdot \nabla \zeta + \eta v_x = \Delta_2 \zeta + R \partial_y \theta, \tag{2.2a}$$

$$P(\partial_t \theta + \boldsymbol{v} \cdot \nabla \theta) = \Delta_2 \theta - v_x, \tag{2.2b}$$

where $\Delta_2 = \partial_x^2 + \partial_y^2$. Introducing the 'local state vector' of the fluid, $V = (\psi, \theta)$, we rewrite these basic equations as

$$\mathrm{D} \cdot \partial_t V + \mathrm{N}_2(V, V) = \mathrm{L}_R \cdot V, \tag{2.2}$$

with the linear operators D and L_R and the nonlinear one N_2. Assuming isothermal cylindrical walls we have as boundary conditions either

$$\partial_y \psi = \partial_x^2 \psi = \theta = 0 \quad \text{at} \quad x = \pm 1/2 \quad \text{in the stress-free case,} \tag{2.3a}$$

or

$$\partial_y \psi = \partial_x \psi = \theta = 0 \quad \text{at} \quad x = \pm 1/2 \quad \text{in the no-slip case.} \tag{2.3b}$$

Because of the annular geometry, the model allows for a non-vanishing mean flow $\overline{v_y}$, where the bar indicates the average over the y-direction. To ensure the periodicity of the pressure in the y-direction, one must supplement the local vorticity equation (2.2a) with the average over y of the azimuthal component of the Navier–Stokes equation,

$$\partial_t \overline{v_y} + \overline{v_x \partial_x v_y} = \partial_x^2 \overline{v_y}, \quad \text{i.e.} \quad -\partial_t \partial_x \overline{\psi} + \overline{v_x \partial_x v_y} = -\partial_x^3 \overline{\psi}. \tag{2.4}$$

The x-derivative of this equation is identical to the y-average of equation (2.2a).

3. Asymptotic theory for the onset of convection

The stability analysis of the purely conductive state, $V = 0$, can be performed through the solution of the linearized eigenvalue problem

$$\sigma \mathrm{D} \cdot V = \mathrm{L}_R \cdot V, \tag{3.1}$$

with the boundary conditions (2.3). Because of the periodicity $y \mapsto y + L$, the eigenmodes are Fourier modes, $\exp(\mathrm{i}\alpha y)$. In accordance with the small-gap approximation α is regarded as a continuous parameter. Solutions of (3.1) corresponding to a vanishing real part of σ, $\sigma = -\mathrm{i}\omega(\alpha)$, are obtained for $R = R(\alpha)$ and called neutral

modes $V = V_1(\alpha)$. The Rayleigh number $R(\alpha)$ takes its minimum at the critical value R_c corresponding to the critical wavenumber α_c and the critical frequency ω_c. Since $\omega_c > 0$ for $\eta > 0$, these modes correspond to progradely travelling thermal Rossby waves.

While explicit analytical solutions of the linear problem (2.3), (3.1) can be obtained in the stress-free case (BO86), only numerical solutions have been obtained in the no-slip case (Schnaubelt & Busse 1992). Numerical difficulties are encountered at large η, which become more dramatic at small P. However, since α_c increases with η, the differences of the solutions for the two types (2.3) of boundary conditions should disappear asymptotically for large η as has already been anticipated by Busse (1970). In order to study this convergence in detail, we first recall in § 3.1 the stress-free linear solutions, before presenting in § 3.2 an asymptotic calculation of the no-slip neutral wave at a prescribed wavenumber α_0. The results will be discussed in § 3.3.

3.1. *Linear solution in the stress-free case*

As shown in BO86, in the stress-free case the thermal Rossby wave

$$\psi = \cos(\pi x)\exp[\mathrm{i}(\alpha y - \omega_{sf}(\alpha)t)], \quad \theta = \frac{-\mathrm{i}\alpha\cos(\pi x)}{\alpha^2+\pi^2-\mathrm{i}\omega_{sf}(\alpha)P}\exp[\mathrm{i}(\alpha y-\omega_{sf}(\alpha)t)] \tag{3.2}$$

with the frequency

$$\omega_{sf}(\alpha) = \frac{\sqrt{2}\eta_p}{P}\frac{\alpha}{\pi^2+\alpha^2}, \quad \text{where} \quad \eta_p = \frac{\eta P}{\sqrt{2}(1+P)} \quad \text{has been defined,} \tag{3.3}$$

is neutral at the Rayleigh number

$$R_{sf}(\alpha) = \frac{(\pi^2+\alpha^2)^3}{\alpha^2} + \frac{2\eta_p^2}{\pi^2+\alpha^2}. \tag{3.4}$$

In the limit of large η_p, the critical wavenumber α_c minimizing $R_{sf}(\alpha)$ approaches the value $\alpha_0 = \eta_p^{1/3}$ corresponding to $R_{sf}(\alpha_0) \sim 3\eta_p^{4/3}$ and $\omega_{sf}(\alpha_0) \sim \sqrt{2}P^{-1}\eta_p^{2/3}$.

3.2. *Asymptotic solution for the no-slip case*

The no-slip neutral mode with wavenumber α_0 can be written in the form

$$\psi = \Psi_1(x;\alpha_0)\exp[\mathrm{i}(\alpha_0 y - \omega_{ns}(\alpha_0)t)], \quad \theta = \Theta_1(x;\alpha_0)\exp[\mathrm{i}(\alpha_0 y - \omega_{ns}(\alpha_0)t)]. \tag{3.5}$$

After elimination of Θ_1 through the use of the linearized vorticity equation, the linearized heat equation (2.2*b*) gives an ordinary differential equation of sixth order for $\Psi_1(x)$, the solutions of which take the form

$$\Psi_1(x) = A\cosh(\lambda x) + A_+\cosh(\lambda_+ x) + A_-\cosh(\lambda_- x). \tag{3.6}$$

In the large-η_p limit, the characteristic polynomial yields two large roots $\lambda_\pm$ which behave asymptotically as

$$\lambda_\pm \sim \eta_p^{1/3}\sqrt{\Lambda_\pm} \tag{3.7a}$$

with

$$\Lambda_\pm = \frac{3-\mathrm{i}\sqrt{2}(1+P^{-1})}{2} \pm \frac{\sqrt{\delta}}{2} \quad \text{and} \quad \delta = -5+4P^{-1}-2P^{-2}-2\mathrm{i}\sqrt{2}(1+P^{-1}), \tag{3.7b}$$

and a small root λ which can be regarded as a perturbation of the stress-free value,

$$\lambda = \mathrm{i}\pi + \mu \quad \text{with} \quad \mu \sim \frac{P\eta_p^{-2/3}R_1 + P[(P-1)\sqrt{2}-(1+P)\,\mathrm{i}]\omega_1}{2\pi[(1+P)\sqrt{2}+(3P-2)\,\mathrm{i}]}, \tag{3.8a}$$

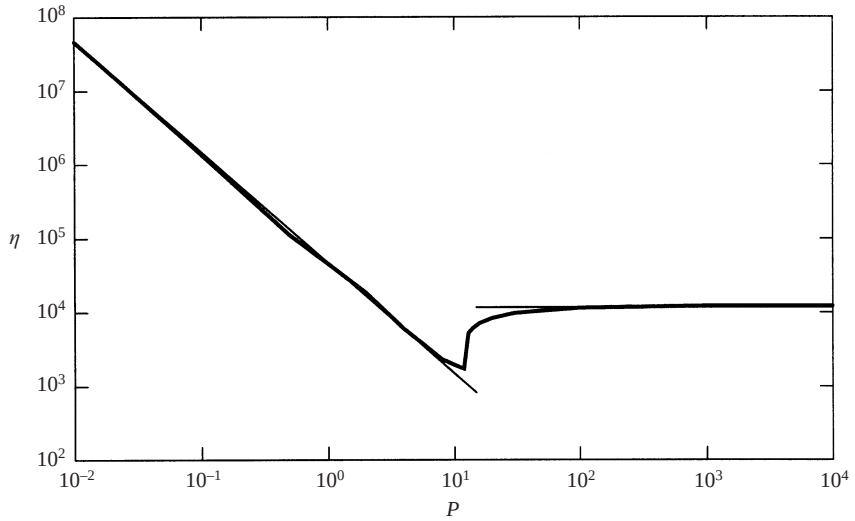

FIGURE 2. The thin lines show the predictions of the asymptotic theory concerning the limit value of η above which the no-slip onset value $R_{ns}(\alpha_0)$ has converged to the stress-free asymptotic onset value R_0, using the convergence criterion $|\delta R/R| < 10^{-3}$ with equation (3.12) on the right (large Prandtl numbers), (3.15) on the left (small Prandtl numbers). The thick line shows the results of the numerical solution of the no-slip linear eigenvalue problem.

where the definitions

$$R_1 = R_{ns}(\alpha_0) - R_{sf}(\alpha_0) \quad \text{with} \quad R_1 \ll R_{sf}(\alpha_0), \tag{3.8b}$$

$$\omega_1 = \omega_{ns}(\alpha_0) - \omega_{sf}(\alpha_0) \quad \text{with} \quad \omega_1 \ll \omega_{sf}(\alpha_0) \tag{3.8c}$$

have been introduced. Since the real parts $\mathrm{Re}(\lambda_\pm)$ are large, the solution (3.6) satisfying the no-slip boundary conditions takes asymptotically the form

$$\Psi_1(x) \sim (\lambda_+ - \lambda_-)\cosh(\lambda x) + 2\exp(-\lambda_+/2)[\lambda_- \cosh(\lambda/2) - \lambda \sinh(\lambda/2)]\cosh(\lambda_+ x)$$
$$+2\exp(-\lambda_-/2)[\lambda \sinh(\lambda/2) - \lambda_+ \cosh(\lambda/2)]\cosh(\lambda_- x). \tag{3.9}$$

Eventually the isothermal boundary condition gives at leading order a complex equation of the form $b_R R_1 + b_\omega \omega_1 = b_0$ from which R_1 and ω_1 can be calculated. Because of their complex dependence on P (see e.g. (3.7)), the explicit general analytical expressions are lengthy and will not be given here. Instead we shall focus on the limits of small and large Prandtl numbers, which cover most of the regions of interest as is evident from figure 2.

3.3. *Comparison of stress-free and no-slip results – discussion*

In the large-Prandtl-numbers limit one finds

$$\Lambda_\pm = (3 - \mathrm{i}\sqrt{2} \pm \sqrt{-5 - 2\mathrm{i}\sqrt{2}})/2, \quad \mu \sim (1.67 + 5.05\,\mathrm{i})\eta^{-1/3}, \tag{3.10}$$

$$R_1 \sim -22.0\eta^{1/3}, \quad \omega_1 \sim -76.4P^{-1}\eta^{-1/3}, \tag{3.11}$$

i.e. the boundary layers are destabilizing. Exact algebraic expressions can be given for μ, R_1 and ω_1, but they are still too lengthy to be displayed. From (3.8*c*) and (3.11)

one deduces the relative corrections to the neutral Rayleigh number and frequency,

$$\frac{\delta R}{R} = \frac{R_1}{R_{sf}(\alpha_0)} \sim -11.6\eta^{-1}, \quad \frac{\delta\omega}{\omega} = \frac{\omega_1}{\omega_{sf}(\alpha_0)} \sim 68.0\eta^{-1}. \tag{3.12}$$

Thus the convergence of the no-slip linear properties towards the stress-free linear properties occurs independently of P for large P. As shown in figure 2, this prediction is confirmed by the fully numerical solution of (3.1) obtained through the use of superpositions of modes with $\exp(\lambda x)$ for $\Psi_1(x)$ and $\Theta_1(x)$ or through the use of a Galerkin scheme (see § 5). Moreover, the neutral wave profiles deduced from (3.9) agree well with the profiles computed numerically. The fact that $\lambda_\pm$ scale with $\eta^{1/3}$ indicates that a Stewartson layer (Greenspan 1968) of thickness $l_x \sim \eta^{-1/3}$ develops in the v_y field.

In the small-Prandtl-numbers limit one finds

$$\Lambda_+ = 1 - \mathrm{i}\sqrt{2}, \quad \Lambda_- = -\mathrm{i}\sqrt{2}P^{-1}, \quad \mu \sim 2^{5/12}\pi(\mathrm{i}-1)P^{1/6}\eta^{-1/3}, \tag{3.13}$$

$$R_1 \sim 3 \times 2^{19/12}\pi^2 P^{-1/6}\eta^{1/3}, \quad \omega_1 \sim -2^{23/12}(1+\sqrt{2})\pi^2 P^{-5/6}\eta^{-1/3}, \tag{3.14}$$

i.e. the boundary layers are stabilizing. Accordingly the relative corrections to the neutral Rayleigh number and frequency are

$$\frac{\delta R}{R} \sim 2^{9/4}\pi^2 P^{-3/2}\eta^{-1}, \quad \frac{\delta\omega}{\omega} \sim -2^{7/4}(1+\sqrt{2})\pi^2 P^{-1/2}\eta^{-1}. \tag{3.15}$$

As P approaches zero, the Coriolis parameter η thus must reach extremely high values to ensure the convergence of the no-slip and the stress-free linear properties, in agreement with the fully numerical computations (figure 2). A salient feature is the Prandtl number dependence of the root Λ_-, which implies that $\lambda_- \sim P^{-1/6}\eta^{1/3}$. For small Prandtl numbers a thermally modified Stewartson layer of thickness $l_x \sim P^{1/6}\eta^{-1/3}$ thus develops in the v_y field. This delayed convergence at small Prandtl numbers is caused by the relatively low values of the wavenumber α_0: the larger the wavelength, the stronger the influence of the boundary conditions.

The calculations presented here are similar to those performed for rotating Rayleigh–Bénard convection by Clune & Knobloch (1993) and by Zhang & Roberts (1998). In addition to the Stewartson layers at the cylindrical walls the Ekman layers at the conical caps of the annulus can also be considered, as has been done by Busse (1970) and Zhang & Jones (1993). The changes in the critical Rayleigh numbers due to Ekman layers and Stewartson layers are in fact additive and thus can be considered independently. Equation (4.9) of Zhang & Jones (1993) shows that the Ekman layers also have a stabilizing effect at small Prandtl numbers and a destabilizing effect at large Prandtl numbers. A comparison with our equations (3.12) and (3.15) proves that in the asymptotic regime the Stewartson layers play a more important role than the Ekman layers when the inequalities

$$((1+P)/P)^{3/2} \ll \eta \ll \eta_0^{3/5}(h/d)^{1/5}(1+P)/P \tag{3.16}$$

are satisfied, which can be realized for long cylinders with $h \gg d$.

4. Weakly nonlinear dynamics: envelope equation

In order to study the nonlinear dynamics of the system near onset, i.e. for $0 < \epsilon = R/R_c - 1 \ll 1$, we construct the Ginzburg–Landau or envelope equation with the spectral method as reviewed for instance by Dangelmayr & Kramer (1998).

4.1. *Construction of the envelope equation*

A general wave packet ansatz has the form

$$W = \int_{\mathscr{V}(0)} \mathrm{d}q \widehat{A}(\alpha_c + q) V_1(\alpha_c + q) \exp(-\mathrm{i}\omega_c t) \sim A(y) V_1(\alpha_c) \exp(-\mathrm{i}\omega_c t), \tag{4.1}$$

where $\mathscr{V}(0)$ indicates the set of the small wavenumbers $q \ll \alpha_c$ and

$$A(y) = \int_{\mathscr{V}(0)} \mathrm{d}q \widehat{A}(\alpha_c + q) \exp(\mathrm{i}qy) \tag{4.2}$$

is the slowly varying envelope. Approximate solutions of the evolution equations (2.2) and (2.4) of the form

$$V = W + W^* + V_\perp \tag{4.3}$$

are sought, with $V_\perp$, regarded as a perturbation of W, in the passive modes subspace generated by the eigenmodes of (3.1) with finite negative growth rate $\mathrm{Re}(\sigma)$. This allows an *adiabatic elimination* of $V_\perp$ at the order A^2.

Accordingly, the nonlinear source terms of wavenumbers close to $\pm 2\alpha_c$ in (2.2) generate the terms

$$A^2(y) V_2(\alpha_c, \alpha_c) \exp(-2\mathrm{i}\omega_c t) + \text{c.c.} \tag{4.4}$$

in $V_\perp$, with

$$V_2(\alpha_c, \alpha_c) = (2\mathrm{i}\omega_c \mathrm{D} + \mathrm{L}_{R_c})^{-1} \cdot \mathrm{N}_2(V_1(\alpha_c) | V_1(\alpha_c))$$

using the notation

$$\mathrm{N}_2(V_a | V_b) = \mathrm{N}_2(V_a, V_b) + \mathrm{N}_2(V_b, V_a).$$

In a similar way, the slowly modulated streamfunction ψ_2 in $V_\perp$ is controlled by the equations deduced from (2.2*a*) and (2.4),

$$\mathrm{N}_{2\psi}(W | W^*) = |A(y)|^2 S'(x) = -\partial_x^4 \psi_2, \tag{4.5}$$

$$\overline{v_x \partial_x v_y (W | W^*)} = \overline{|A(y)|^2} S(x) = -\partial_x^3 \overline{\psi_2}, \tag{4.6}$$

where

$$S(x) = 2\alpha_c \mathrm{Im}[\Psi_1(x;\alpha_c) \partial_x^2 \Psi_1^*(x;\alpha_c)] = 2\alpha_c \mathrm{Im} \partial_x [\Psi_1(x;\alpha_c) \partial_x \Psi_1^*(x;\alpha_c)]. \tag{4.7}$$

Separating ψ_2 into its mean and fluctuating contributions, $\psi_2 = \bar{\psi}_2 + \varphi_2$ with $\bar{\varphi}_2 = 0$, subtracting ∂_x(4.6) from (4.5) yields

$$[|A(y)|^2 - \overline{|A(y)|^2}] S'(x) = -\partial_x^4 \varphi_2. \tag{4.8}$$

In the stress-free case where, according to (3.2), $\Psi_1(x;\alpha_c) = \cos(\pi x)$ is real, S vanishes, and therefore $\psi_2 = 0$, i.e. there is no large-scale flow at this order. In the no-slip case, however, $\Psi_1(x;\alpha_c)$ is complex once $\eta \neq 0$, which means that the boundaries of the convection cells at a given instant of time are no longer lines $y =$ constant (see figure 5). Thus $S(x)$ is non-vanishing once $\eta \neq 0$. The solution of (4.8) subject to the no-slip boundary conditions (2.3*b*) yields

$$\varphi_2 = [|A(y)|^2 - \overline{|A(y)|^2}] \Psi_2(x) \tag{4.9}$$

with $\Psi_2''''(x) = -S'(x)$, $\Psi_2(\pm 1/2) = \Psi_2'(\pm 1/2) = 0$. The comparison of (4.6) and (4.8) then shows that, since $\partial_x \overline{\psi}_2$ must vanish at $x = \pm 1/2$,

$$\bar{\psi}_2 = \overline{|A(y)|^2} [\Psi_2(x) + M_2(4x^3/3 - x)], \tag{4.10}$$

where the value of M_2 can be deduced after averaging (4.6) over the x-direction, as indicated by angular brackets,

$$M_2 = -\tfrac{1}{8}\langle \Psi_2'''(x)\rangle = -\tfrac{1}{4}\Psi_2''(\tfrac{1}{2}) \tag{4.11}$$

since $\Psi_2(x)$ is odd. Summing (4.9) and (4.10), one finds

$$\psi_2 = |A(y)|^2\Psi_2(x) + \overline{|A(y)|^2}\, M_2(4x^3/3 - x), \tag{4.12}$$

corresponding to the superposition of a typically -if $A(y)$ does depend on y- *'modulated' mean flow* on top of a *'global' Poiseuille mean-flow*.

The slowly modulated temperature field θ_2 in $V_\perp$ is controlled by the equation deduced from (2.2b):

$$\partial_x^2\theta_2 = \mathrm{N}_{2\theta}(W|W^*) = |A(y)|^2\,\mathrm{N}_{2\theta}(V_1(\alpha_c)|V_1(-\alpha_c))$$

which yields

$$\theta_2 = |A(y)|^2\Theta_2(x). \tag{4.13}$$

Introducing the vectors

$$V_2(\alpha_c,-\alpha_c) = (\Psi_2(x),\Theta_2(x)) \quad \text{and} \quad V_{gm} = M_2(4x^3/3 - x, 0),$$

one can combine (4.4), (4.12) and (4.13) to give

$$V_\perp = [A^2(y)V_2(\alpha_c,\alpha_c)\exp(-2\mathrm{i}\omega_c t) + \text{c.c.}] + |A(y)|^2V_2(\alpha_c,-\alpha_c) + \overline{|A(y)|^2}\, V_{gm}. \tag{4.14}$$

This result for the no-slip case includes formally the simpler stress-free case if one sets $\Psi_2 = M_2 = V_{gm} = 0$.

After projection of (2.2) onto the adjoint mode $U_1(\alpha_c+q)$ as shown in the Appendix, multiplication by $\exp[\mathrm{i}(qy+\omega_c t)]$ and integration, the linear terms of (2.2) yield

$$\partial_t A(y) = \int_{\mathscr{V}(0)} \mathrm{d}q\widehat{A}(\alpha_c+q)[\sigma(\alpha_c+q,R) + \mathrm{i}\omega_c]\exp(\mathrm{i}qy)$$

with

$$\begin{aligned}\sigma(\alpha_c+q,R) &= \langle U_1(\alpha_c+q), \mathrm{L}_R\cdot V_1(\alpha_c+q)\rangle \\ &\sim -\mathrm{i}\omega_c + \sigma_0(1+\mathrm{i}s)\epsilon - \mathrm{i}v_g q - \beta(1+\mathrm{i}b)q^2\end{aligned} \tag{4.15}$$

for small q and ϵ, where $v_g = \partial_\alpha\omega$ is the group velocity of the waves at $\alpha = \alpha_c$, and σ_0 and β are positive numbers. Using classical Fourier-transform rules, one obtains

$$\partial_t A(y) \sim \sigma_0(1+\mathrm{i}s)\epsilon A(y) - v_g\partial_y A(y) + \beta(1+\mathrm{i}b)\partial_y^2 A(y). \tag{4.16}$$

Eventually the same treatment of the *resonant nonlinear terms* $\mathrm{N}_2(W|V_\perp)+\mathrm{N}_2(W^*|V_\perp)$ in (2.2) yields at lowest order the terms

$$-(\gamma_r+\mathrm{i}\gamma_i)|A(y)|^2A(y) - (\delta_r+\mathrm{i}\delta_i)\overline{|A(y)|^2}\, A(y) \tag{4.17}$$

with

$$\gamma_r + \mathrm{i}\gamma_i = \langle U_1(\alpha_c), \mathrm{N}_2(V_1(\alpha_c)|V_2(\alpha_c,-\alpha_c)) + \mathrm{N}_2(V_1(-\alpha_c)|V_2(\alpha_c,\alpha_c))\rangle, \tag{4.18}$$

$$\delta_r + \mathrm{i}\delta_i = \langle U_1(\alpha_c), \mathrm{N}_2(V_1(\alpha_c)|V_{gm})\rangle. \tag{4.19}$$

Adding (4.16) and (4.17) we obtain the *envelope equation*

$$\begin{aligned}\partial_t A(y) + v_g\partial_y A(y) = \sigma_0(1+\mathrm{i}s)\epsilon A(y) + \beta(1+\mathrm{i}b)\partial_y^2 A(y) - (\gamma_r+\mathrm{i}\gamma_i)|A(y)|^2A(y) \\ -(\delta_r+\mathrm{i}\delta_i)\overline{|A(y)|^2}\, A(y).\end{aligned} \tag{4.20}$$

The group velocity term $\propto v_g$ can be removed by changing to a moving frame. Moreover the introduction of slow scales according to $t' = \epsilon t, y' = \epsilon^{1/2}(y - v_g t)$ and of a normalized amplitude according to $A = \epsilon^{1/2} A'$ proves that all the other terms summed in (4.20) are of the same order $\epsilon^{3/2}$.

In the stress-free case, where all the above calculations can be done analytically, we have $\delta_r = \delta_i = 0$, and thus recover the standard envelope equation (4.1) or (4.3) of HB97. In the no-slip case we must carry out numerical calculations, either using superpositions of modes in $\exp(\lambda x)$, or employing the Galerkin scheme (§ 5). The global mean-flow coefficient $\delta_r + \mathrm{i}\delta_i$ is non-vanishing once $\eta \neq 0$ and the corresponding nonlinear term introduces a global (or non-local) coupling. To our knowledge, such modified forms of the Ginzburg–Landau equation have only been considered in the case of a stationary bifurcation, with purely real coefficients in (4.20) (Hall 1984; Elmer 1988), or in the case of non-dissipative waves, with purely imaginary coefficients (Pierce & Knobloch 1994). In our more general case of complex coefficients, we shall see that the global-coupling term gives rise to rather special stability properties. First, however, the sign and the magnitude of the coefficients of (4.20) must be specified, as we shall do through evaluation of the structure of the spatially periodic Rossby wave in the neighbourhood of the onset of convection.

4.2. *Structure of the critical wave in the no-slip case*

The weakly nonlinear solution of (2.2) with the critical wavenumber α_c is obtained as the special case $\widehat{A}(\alpha_c + k) = A_0 \delta(k)$ in the wave packet expansion (4.1), which thus reduces to $W = A_0 V_1(\alpha_c)$. At leading order this corresponds naturally to a sinusoidal wave.

The quadratic order yields, according to (4.14),

$$V_\perp = [A_0^2 V_2(\alpha_c, \alpha_c) \exp(-2\mathrm{i}\omega_c t) + \text{c.c.}] + |A_0|^2 [V_2(\alpha_c, -\alpha_c) + V_{gm}]. \tag{4.21}$$

The mode $V_2(\alpha_c, -\alpha_c)$ includes an antisymmetric temperature profile $\Theta_2(x)$ that describes the enhancement of the heat transport due to convection, as measured by the Nusselt number

$$Nu = 1 + P\overline{\partial_x \theta|_{x=-1/2}} = 1 + P|A_0|^2 \Theta_2'(-\tfrac{1}{2}). \tag{4.22}$$

For $\eta = 0$, $\Theta_2(x)$ generated by the heat-advection terms $P\boldsymbol{v} \cdot \nabla\theta$ in the heat equation (2.2*b*) is proportional to P. Because A_0 tends to a finite value as $P \to 0$ in the no-slip case, this explains why Nu decreases rapidly in proportion to P^2 for $P \leqslant 1$ and $\eta = 0$ (figure 3). On the other hand, the stress-free case value of the reduced Nusselt number, $(Nu - 1)/\epsilon = 2$ (equation (3.14) of BO86), is recovered at quite large η.

More specific for our rotating system is the generation of the mean flow

$$u(x) = \overline{v_y(x, y, t)} = -\partial_x \overline{\psi_2} = |A_0|^2 [-\Psi_2'(x) + M_2(1 - 4x^2)] = |A_0|^2 u_2(x), \tag{4.23}$$

with a typical profile shown in figure 4(*a*). Since $u'(\pm 1/2) = 0$ according to (4.11), no torque is exerted on the boundaries of the annular layer. We note also that in the stress-free case a mean flow appears only at the quartic order (see equation (3.10) of BO86; see also the large-η asymptotic results of Abdulrahman *et al.* 2000) and presents a different profile (it is prograde in the interior of the layer). There is a connection between the quadratic mean flow and the geometry of the separatrices between convection cells in the linear wave flow, defined by the equation

$$\psi_1 = 0, \quad \text{i.e.} \quad \Psi_{1r}(x; \alpha_c) \cos(\alpha_c y) - \Psi_{1i}(x; \alpha_c) \sin(\alpha_c y) = 0.$$

Indeed by differentiation of this equation, multiplication by $\Psi_{1r}(x) \sin(\alpha_c y)$ and

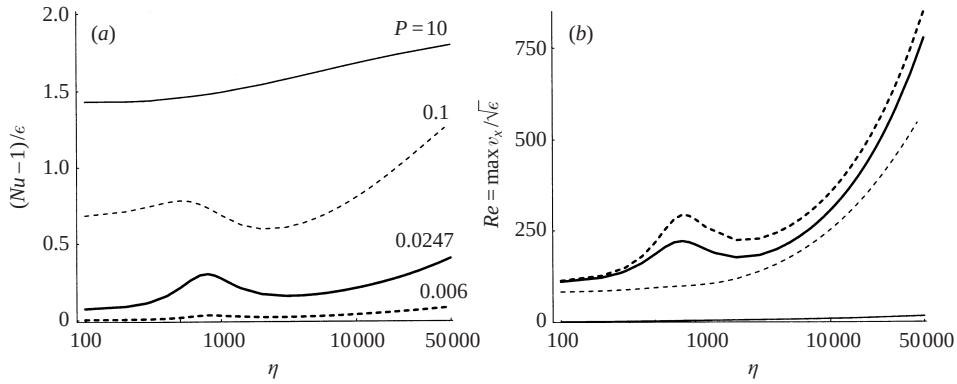

FIGURE 3. (*a*) The reduced Nusselt number deduced from (4.22), (4.28) is plotted vs. η for four different values of P as indicated. (*b*) The wave amplitude or reduced Reynolds number (4.29) is plotted vs. η for the same values of P.

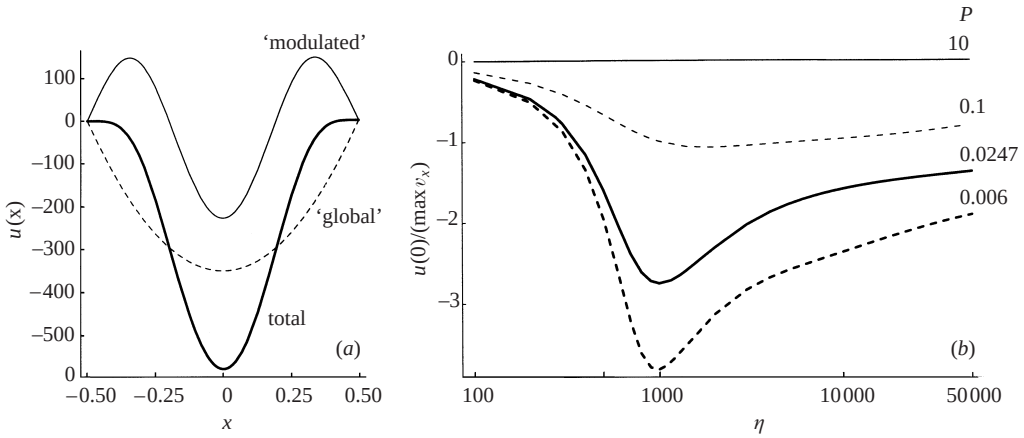

FIGURE 4. (*a*) For $P = 0.0247$, $\eta = 1000$, the thick line shows the mean-flow profile predicted at $\epsilon = 1$ according to (4.23), (4.28). The thin (resp. dashed) line shows the contribution of the term $\propto \Psi_2(x)$ (resp. $1 - 4x^2$) to this profile. Note that in a more general case where $A(y)$ would depend on y the contribution of the term $\propto \Psi_2(x)$ would correspond to the 'modulated' mean flow, and the contribution of the term $\propto 1 - 4x^2$ to the 'global' mean flow, see (4.12) and the corresponding discussion. (*b*) For four different values of P as indicated on the right, the ratio of the mid-layer mean-flow amplitude at $\epsilon = 1$ vs. the maximum wave-flow amplitude at $\epsilon = 1$ equation (4.30) is plotted as a function of η.

simplification by $\sin^2(\alpha_c y)$, one obtains that, along a separatrix with equation $y(x)$,

$$\alpha_c |\Psi_1(x)|^2 \, \mathrm{d}y = [\Psi'_{1r}(x)\Psi_{1i}(x) - \Psi_{1r}(x)\Psi'_{1i}(x)] \, \mathrm{d}x. \tag{4.24}$$

On the other hand (4.6) and (4.7) lead to

$$u''_2(x) = S(x) = 2\alpha_c \partial_x [\Psi'_{1r}(x)\Psi_{1i}(x) - \Psi_{1r}(x)\Psi'_{1i}(x)], \tag{4.25a}$$

i.e.

$$u'_2(x) = 2\alpha_c [\Psi'_{1r}(x)\Psi_{1i}(x) - \Psi_{1r}(x)\Psi'_{1i}(x)] = 2\alpha_c^2 |\Psi_1(x)|^2 y'(x) \tag{4.25b}$$

because of the boundary conditions $u'_2 = \Psi_1 = 0$ at $x = \pm 1/2$. This relationship between the mean flow and the slope of the separatrices $y'(x)$, which indicates a 'tilt' of the convection cells, is illustrated in figure 5.

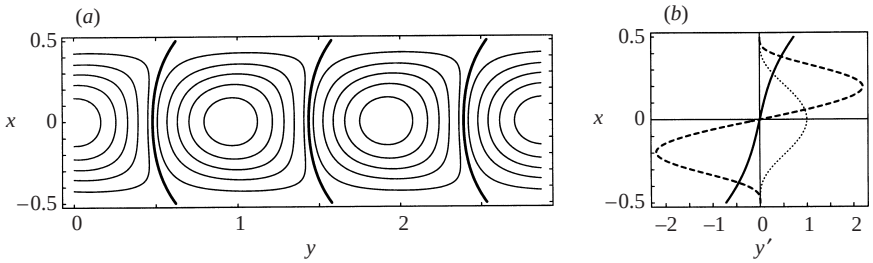

FIGURE 5. For $P = 0.0247$, $\eta = 1000$: (*a*) The lines of constant streamfunction of the linear wave mode, with the thick lines indicating the separatrices $y(x)$ defined by $\psi_1 = 0$. (*b*) The relation with the mean flow (4.25) is illustrated by a dotted line for the factor $|\Psi_1(x)|^2$, a solid line for the factor $y'(x)$ and a dashed line for the result $u_2'(x)$.

The value of the amplitude A_0 is controlled by the balance between the linear and nonlinear terms in (4.20), which reduces here to the amplitude equation

$$\partial_t A_0 = \sigma_0(1+\mathrm{i}s)\epsilon A_0 - \gamma(1+\mathrm{i}c)|A_0|^2 A_0 \quad \text{with} \quad \gamma(1+\mathrm{i}c) = \gamma_r + \mathrm{i}\gamma_i + \delta_r + \mathrm{i}\delta_i. \tag{4.26}$$

The saturation coefficient

$$\gamma = \gamma_r + \delta_r \tag{4.27}$$

is always positive, indicating a supercritical bifurcation, i.e.

$$|A_0(\epsilon)| = \sqrt{\sigma_0\epsilon/\gamma}. \tag{4.28}$$

At large P, the global mean-flow contribution δ_r to the saturation coefficient (4.27) is negligible, and the saturation arises from the advection of the mean temperature profile $\Theta_2(x)$, i.e. from the contribution of $Pv_x\partial_x\Theta_2$ to γ_r. This contribution increases with increasing P and explains the small convection velocities at large P (figure 3) as measured by the Reynolds number

$$Re = \max v_x/\sqrt{\epsilon} = 2\alpha_c|A_0(1)| = 2\alpha_c\sqrt{\sigma_0/\gamma}. \tag{4.29}$$

The value in the stress-free case for large η deduced from (3.1) and (3.7) of BO86, $Re \sim 2^{3/2}3^{1/2}P^{-1}\eta_p^{1/3}$, is recovered only at rather large η, especially for small P. The smallness of $|A_0(1)|$ at large P also implies that the relative strength of the mean flow

$$u(0)/\max v_x(\epsilon = 1) = |A_0(1)|/(2\alpha_c)u_2(0) = Re/(4\alpha_c^2)u_2(0) \tag{4.30}$$

according to (4.23) decreases with increasing P as shown in figure 4(*b*).

At small P (and not too small η), the global mean-flow contribution δ_r to the saturation coefficient (4.27) dominates the γ_r term which can even become negative, see the corresponding parameter region in figure 7. There the γ_r term is dominated by the contribution due to the 'modulated' mean-flow $\propto \Psi_2(x)$ in (4.18), which adds to the excitation of the prograde-travelling waves through the advection of these waves in the regions where this mean flow is also prograde, i.e. near the cylindrical walls (see figure 4*a*). This creates a local minimum of γ around $\eta \simeq 1000$ which is visible in the form of bumps on the curves for $P = 0.006$ and $P = 0.0247$ in figure 3.

The full complex solution of (4.26) reads

$$A_0(\epsilon) = \sqrt{\sigma_0\epsilon/\gamma}\ \exp(-\mathrm{i}\Delta\omega t) \quad \text{with the frequency shift} \quad \Delta\omega = (c-s)\sigma_0\epsilon, \tag{4.31}$$

which contains a linear term proportional to s (originating from (4.15)) as well as a

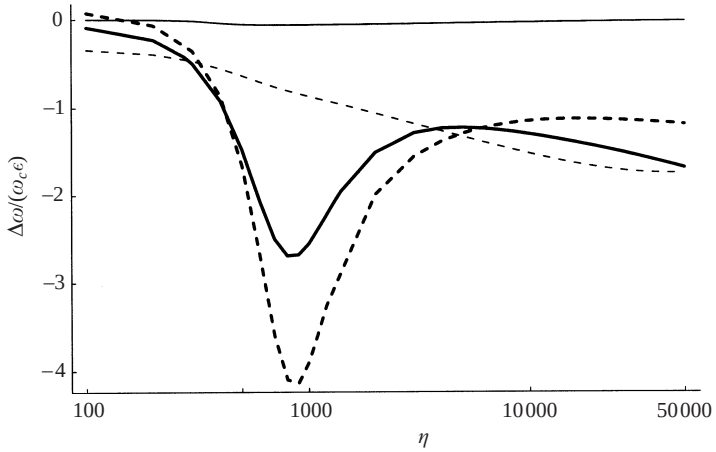

FIGURE 6. The relative frequency shift deduced from (4.31) is plotted vs. η for four different values of P as in figure 4(b).

nonlinear term proportional to

$$c = (\gamma_i + \delta_i)/(\gamma_r + \delta_r). \tag{4.32}$$

In sharp contrast to the stress-free case, where one finds that $\Delta\omega = 0$ at this order (since $s = c = \gamma_i/\gamma_r$), there exists a strong slowing down of the waves in the no-slip case for small P and intermediate η (figure 6), caused by the global mean-flow term $\propto \delta_i$ (one has $\delta_i < 0$, $|\delta_i| \gg |\gamma_i|$ and $|s| \ll |c|$). Indeed, through advection the retrograde mean flow slows down the prograde propagation of the wave.

4.3. *General stability analysis of the critical wave*

Near onset the critical wave may be destabilized by sideband modulational instabilities corresponding to growing modes with wavenumbers $\alpha_c \pm p$ with $p \ll \alpha_c$. Using the ansatz

$$\widehat{A}(\alpha_c+q) = A_0\delta(q)+a_+\delta(q-p)+a_-\delta(q+p), \quad \text{i.e.} \quad A(y) = A_0+a_+\exp(\mathrm{i}py)+a_-\exp(-\mathrm{i}py)$$

with infinitesimal amplitudes $a_\pm$, we obtain after introduction into (4.20) a 2×2 system describing the evolution of the amplitudes a_+ and a_-, with the growth rates

$$\mathrm{Re}(\sigma_\pm) = -\beta p^2 - \frac{\gamma_r\sigma_0\epsilon}{\gamma} \pm \frac{1}{\gamma}\mathrm{Re}[\sqrt{(\gamma_r\sigma_0\epsilon)^2 - 2\beta b\gamma_i\gamma\sigma_0\epsilon p^2 - (b\beta\gamma p^2)^2}]. \tag{4.33}$$

Naturally the global mean-flow coefficients δ_r and δ_i do not appear since they do not control the dynamics of wave modulations; on the contrary the sign of the 'modulated' contribution γ_r to the saturation coefficient $\gamma = \gamma_r + \delta_r$ appears to be crucial.

In the case $\gamma_r > 0$ where the 'modulated flows' saturate, one finds for the maximum growth rate

$$\mathrm{Re}(\sigma_+) = -\beta(1 + b\gamma_i/\gamma_r)p^2 + O(p^4). \tag{4.34}$$

Hence a criterion similar to the Newell criterion (Newell 1974) is recovered:

$$\text{critical wave is } \textit{unstable} \iff 1 + b\gamma_i/\gamma_r < 0. \tag{4.35}$$

In the classical case $\delta_r = \delta_i = 0$ (no global-coupling term in (4.20)), where $\gamma_r > 0$ is assumed to ensure supercriticality and the nonlinear phase shift (4.32) reduces to

$c = \gamma_i/\gamma_r$, the criterion (4.35) reduces to the classical Newell criterion determined by the sign of $1 + bc$. This simplification no longer holds in the case $\delta_r + \mathrm{i}\delta_i \neq 0$.

In the case $\gamma_r = 0$ where the 'modulated flows' do not feed back onto the amplitudes, the sign of the product $b\gamma_i$ is decisive. For $b\gamma_i > 0$ the maximum growth rate is

$$\mathrm{Re}(\sigma_+) = \mathrm{Re}(\sigma_-) = -\beta p^2 + O(p^4), \quad \text{i.e. the critical wave is } \textit{stable}. \tag{4.36}$$

On the other hand, for $b\gamma_i < 0$ the maximum growth rate becomes

$$\mathrm{Re}(\sigma_+) = \left(\frac{-2\beta b\gamma_i\sigma_0\epsilon}{\gamma}\right)^{1/2} |p| + O(p^2), \quad \text{i.e. the critical wave is } \textit{unstable}. \tag{4.37}$$

Note that the growth rate is non-analytic in the limit $p \to 0$.

Finally, in the case $\gamma_r < 0$ where the 'modulated flows' exert a positive feedback,

$$\mathrm{Re}(\sigma_+) = -\frac{2\sigma_0\epsilon\gamma_r}{\gamma} + \beta\left(b\frac{\gamma_i}{\gamma_r} - 1\right)p^2 + O(p^4), \tag{4.38}$$

i.e. the critical wave is always unstable. Note that for $p \to 0$, $\mathrm{Re}(\sigma_-)$ tends to a finite positive limit. This corresponds to an 'amplitude instability' which is linked to the fact that the bifurcation without the global Poiseuille mean flow would be subcritical.

4.4. *Stability results for the rotating annulus model*

In the stress-free case where the global mean-flow term vanishes ($\delta_r = \delta_i = 0$), the stability properties of the critical wave near onset are simply ruled by the Newell criterion (4.35), and the results of HB97 are recovered. As shown in their figure 6, there exists for small P and intermediate η a zone of instability at onset, which is caused by the property that in (4.35) b attains large negative values whereas γ_i/γ_r is of the order of $+1$.

In the no-slip case, using the modified Newell criterion (4.35), we find the stability diagram shown in figure 7. Two different unstable regions can be distinguished. Region I is analogous to the region found in the stress-free case (figure 6 of HB97). Here b is negative and γ_i is positive; except for very low P, γ_r is small but positive, thus $\gamma_i/\gamma_r > 0$. However this region I extends only up to $P \simeq 0.12$, whereas in the stress-free case unstable waves at onset may exist up to $P \simeq 0.20$. For intermediate values of η, the no-slip boundaries thus have a stabilizing influence. For $P \leqslant 0.026$, there appears a region where $\gamma_r < 0$. A 'strong' instability of the waves occurs there with perturbation growth rates of the form (4.38), where the coefficient of the p^2 term is positive since γ_r stays small. Note that, in contrast to the stress-free case, the lower boundary of region I approaches a finite value $\eta = 254$ for $P \to 0$.

An unexpected result is the existence of the unstable region II at high η, which is generated by positive values of b and γ_r and negative values of γ_i. This region, which has no analogue in the stress-free case, cannot connect with region I where $b < 0$ and $\gamma_i > 0$. The lower boundary of region I and the upper boundary of region II present a singular behaviour in the limit $P \to 0$. Note that in the limit $\eta \to +\infty$ the waves become stable as expected from the results in the stress-free case. But η must be increased rapidly with decreasing P in order that this stable regime is attained.

Numerical simulations of (4.20) in the unstable regimes shown in figure 7 demonstrate a transition to modulated waves for not too large periodicity intervals L, and to modulated waves with 'phase' or 'defect' turbulence for large L. Once the perturbations have grown the dynamics of (4.20) thus seems to be qualitatively the same as in the case of the standard Ginzburg–Landau equation (see e.g. Dangelmayr & Kramer 1998).

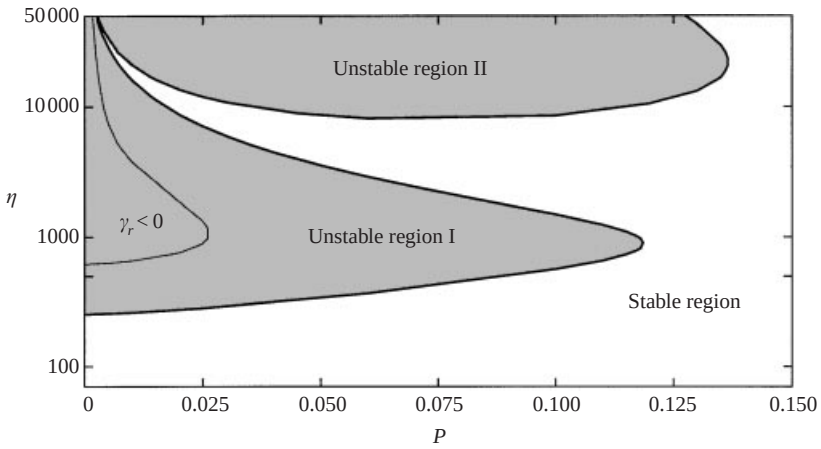

FIGURE 7. The thick line defined by the modified Newell criterion (4.35), $b\gamma_i/\gamma_r = -1$, separates the white region where the critical wave is stable at onset from the shaded regions where it is unstable at onset. The thin line shows the boundary $\gamma_r = 0$.

5. Fully nonlinear dynamics

The weakly nonlinear analysis presented in the previous section is only valid in the small-amplitude regime $\epsilon \ll 1$. In order to solve numerically the evolution equations (2.2) for larger ϵ, we use the Galerkin method.

To resolve the sharp boundary layers that exist at small P (§ 3.3), we use for the nonlinear waves the ansatz

$$\psi = \sum_{m,n} a_{mn} C_n(x) \exp[\mathrm{i}m(\alpha y - \omega t)] + F(x), \quad \theta = \sum_{m,n} b_{mn} S_n(x) \exp[\mathrm{i}m(\alpha y - \omega t)], \quad (5.1)$$

where the C_n and S_n are combinations of Tchebyshev polynomials satisfying the boundary conditions $C_n(\pm 1/2) = C_n'(\pm 1/2) = S_n(\pm 1/2) = 0$. Since the mean-flow part of the streamfunction

$$\overline{\psi}(x) = \sum_n a_{0n} C_n(x) + F(x)$$

must satisfy the global equation (2.4) and the boundary conditions deduced from (2.3*b*), we find for the global mean flow, in analogy to the derivation in § 4.1,

$$F(x) = -\frac{1}{8} \sum_n a_{0n} \langle C_n'''(x) \rangle (4x^3/3 - x), \quad (5.2)$$

which is equivalent to equation (2.6*c*) of Schnaubelt & Busse (1992). The series in (5.1) are truncated with

$$1 \leqslant n \leqslant N_x, \quad -N_y \leqslant m \leqslant N_y. \quad (5.3)$$

After introducing the representation (5.1) in (2.2) and projecting the latter onto the system of expansion functions, we obtain a nonlinear system of equations for the coefficients a_{mn}, b_{mn}, which can be solved with a Newton–Raphson method. The arbitrary phase of the solution is fixed through the choice $\mathrm{Re}(a_{11}) = 0$, to avoid a numerical drift of the waves and to provide an equation determining the frequency ω. The convergence of the computations is tested by the requirement that the Nusselt

number and the frequency change by less than 2% when N_x and N_y are replaced by $N_x - 2$ and $N_y - 2$.

To test the stability of the nonlinear waves (5.1), infinitesimal disturbances of the form

$$\tilde{\psi} = \sum_{m,n} \tilde{a}_{mn} C_n(x) \exp[\mathrm{i}m(\alpha y - \omega t)]\widetilde{W}, \quad \tilde{\theta} = \sum_{m,n} \tilde{b}_{mn} S_n(x) \exp[\mathrm{i}m(\alpha y - \omega t)]\widetilde{W}, \quad (5.4)$$

are superimposed with $\widetilde{W} = \exp(\mathrm{i}py + \tilde{\sigma}t)$ where $p \neq 0$ is the modulation wavenumber. The solution of the linearized equations for the unknowns $\tilde{a}_{mn}$ and $\tilde{b}_{mn}$ yields a finite spectrum of eigenvalues $\{\tilde{\sigma}\}$. Because of the symmetry of the nonlinear wave (5.1), for which $a_{mn} = b_{mn} = 0$ when $m + n$ is odd, the disturbances (5.4) can be separated into two classes: the *even* disturbances for which

$$\tilde{a}_{mn} = \tilde{b}_{mn} = 0 \quad \text{for} \quad m + n = \text{odd} \quad (5.5)$$

holds, and the *odd* disturbances with

$$\tilde{a}_{mn} = \tilde{b}_{mn} = 0 \quad \text{for} \quad m + n = \text{even}, \quad (5.6)$$

where it should be mentioned that C_n and S_n are changed by the factor $(-1)^{n-1}$ when x is replaced by $-x$. The wave (5.1) is unstable once a solution of the form (5.4) with positive growth rate $\mathrm{Re}(\tilde{\sigma})$ exists; a classification of the possible instabilities has been given in Schnaubelt & Busse (1992) and in HB97.

Using stress-free boundary conditions, HB97 have predicted (their figure 4) that for small Prandtl numbers the region of sideband instability at onset (analogous to our region I figure 7) extends into the nonlinear regime. Therefore modulated waves are expected to be observed at small P, intermediate η and not too large R (§6 of HB97). At higher R, owing to an odd-mode short-wavelength instability called the resonance instability, amplitude vacillations are expected in the stress-free case, followed by a chaotic convection state (§7 of HB97). These predictions have motivated the experimental work of Jaletzky (1999), who has investigated convection in a rotating cylindrical annulus filled with mercury. Although the Prandtl number is $P = 0.0247$ in this case, in all experiments at various R and η values, only pure monofrequency waves have been observed.

An important result of our no-slip Galerkin computations is that, at intermediate values of η, the waves typically restabilize at sufficiently high R with respect to both the sideband and the resonance instabilities. As seen in figure 8, this process is associated with a sudden upturn of the Nusselt number vs. Rayleigh number curve, which becomes S-shaped for large η. In this latter hysteretic case, where two turning points appear on the Nusselt number vs. Rayleigh number curve, we follow the solution branch in the numerical scheme by treating R as variable and a_{11} as control parameter. A typical stability diagram is shown on figure 9. With increasing R, the resonance instability typically sets in when the first turning point is approached. The restabilization against both the resonance and sideband instabilities is also connected with the S-shape, since it only happens above the second turning point. These results are in line with Jaletzky's experiments: because of the experimental protocol, the scanned values of R and η are related by $R \propto \eta^2$, and because of a sufficiently large signal to noise ratio only the stable region (thick lines in figure 8) could be probed.

The S-shaped $Nu(R)$ dependence becomes more pronounced as the Prandtl number decreases. As shown in figure 10, nonlinear convection can even be observed for $R < R_c$ in spite of the supercritical character of the first bifurcation. When P approaches zero, arbitrarily large hysteresis gaps are obtained at intermediate values

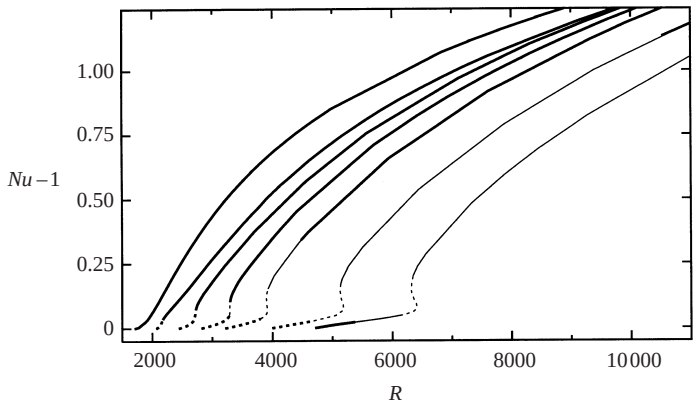

FIGURE 8. Nusselt number vs. Rayleigh number for the nonlinear wave with the critical wavenumber $\alpha_c(\eta)$ for $P = 0.0247$, $\eta = 0$, 1500, 2500, 3400, 4300, 6000, 7500 from left to right. The thick lines denote stable waves, the thick dashed lines indicate waves unstable to sideband instabilities, the thin lines indicate waves unstable to the resonance instability, and the thin dashed lines indicate waves unstable to both modes of instabilities.

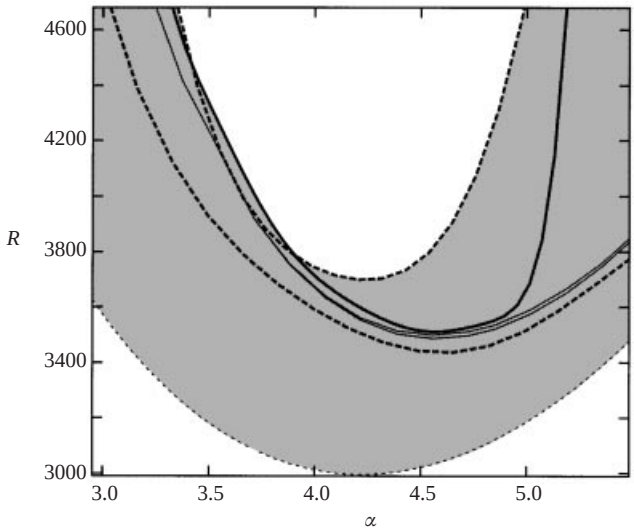

FIGURE 9. Region of instability (shaded) of the waves in the wavenumber–Rayleigh number plane for $P = 0.0247$, $\eta = 3800$. The thin dashed line denotes the neutral curve $R_0(\alpha)$, the thick line describes the upper bound of the sideband instability domain, and the thick dashed lines indicate the boundaries of the resonance instability domain. For $\alpha > 3.7$, the hysteresis domain associated with the S-shapes as seen on figure 8 is indicated with the thin lines. For smaller α the S-shape disappears; here the thin line indicates where $\partial Nu/\partial R$ reaches its maximum value.

of η. A salient feature is the property that, for very small P, the nonlinear waves restabilize both against the sideband and resonance instabilities immediately after the second turning point, which suggests that it corresponds to a *saddle-node bifurcation.*

6. Concluding remarks

An important result is the stabilizing influence of the rigid boundaries in the nonlinear regime of convection in a rotating cylindrical annulus at small Prandtl

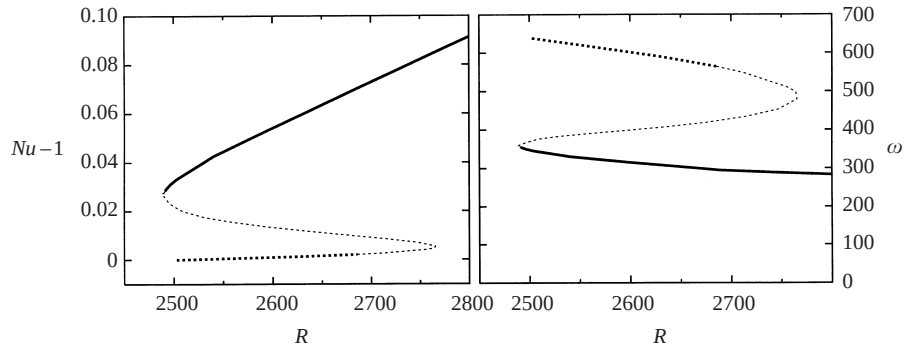

FIGURE 10. Reduced Nusselt number (a) and frequency (b) of the nonlinear wave of critical wavenumber for $P = 0.006$, $\eta = 4300$. The stability properties of this wave are indicated through the use of different lines as in figure 8.

numbers as shown on figure 9. A comparison with figure 6e of Elmer (1988) suggests that this restabilization is related to the mean-flow global-coupling effect that we have demonstrated. The hysteretic transition expected near onset at intermediate values of η (figure 10) is another interesting feature which could eventually be studied experimentally if more precise techniques for measurements of small amplitudes of convection are used. The currently available experimental data (Jaletzky 1999) do not show this feature, but are in agreement with the theory otherwise.

The global-coupling role of mean flows has been taken into account only implicitly up to now, see e.g. Clever & Busse (1989) or Clune & Knobloch (1993), where on the other hand the alternative of a mean pressure gradient in the direction of the mean flow has also been considered. As an example of another system where the envelope equation (4.20) should provide the appropriate theoretical description, we mention the case of rotating Rayleigh–Bénard convection as studied by Liu & Ecke (1997). They used an envelope equation without the global mean-flow coupling term to describe their experimental observations, and found good agreement. This is probably explained by the fact that the Prandtl number was relatively large in the experiment, $P = 6.3$, while mean-flow effects are important only at small Prandtl numbers (figure 4b). We expect that the same experiment carried out with a fluid of small Prandtl number will require an extension of the envelope equation to the form (4.20); accordingly the related theoretical results of Kuo & Cross (1993) or Hecke & Saarloos (1997) should also be revisited.

In order to obtain a closer analogy with the case of spherical convection, curvature effects can be included in the rotating cylindrical annulus model by a modification of the η term in (2.2a), see e.g. BO86, Busse & Hood (1982) (alternately one may consider a large gap and use cylindrical operators as in Pino, Mercader & Net (2000)). The effect of a small curvature is generally to introduce a small antisymmetric component of the linear streamfunction and hence an antisymmetric mean flow (Busse & Hood 1982). With rigid boundaries, the weakly nonlinear scheme of § 4.1 is still valid, except for the lack of $x \mapsto -x$ symmetry, i.e. now $\langle \Psi_2'''(x)\rangle \neq 2\Psi_2''(1/2)$. Accordingly u_2' no longer vanishes at the boundaries, and equation (4.25) linking the quadratic mean flow with the slope of the linear convection cells generalizes to

$$u_2'(x) = 2\alpha_c^2[|\Psi_1(x)|^2 y'(x) - \langle |\Psi_1(x)|^2 y'(x)\rangle] \tag{6.1}$$

where we have used $\langle u_2'(x)\rangle = 0$. A reinvestigation of the strongly nonlinear dynamics in this case and for very low Prandtl numbers would be interesting.

We thank M. Jaletzky for communicating his experimental results, and anonymous referees for their valuable suggestions.

Appendix. Projection technique for the envelope equation

The Hermitian scalar product in V-space is defined by

$$\langle U, V\rangle = \frac{1}{L}\int_{-L/2}^{L/2} \mathrm{d}y \int_{-1/2}^{1/2} \mu(x)\,\mathrm{d}x U^*(x,y)\cdot V(x,y) \tag{A 1}$$

with $\mu(x) = 1$ (resp. $2/\pi/\sqrt{1-(2x)^2}$) if superpositions of modes in $\exp(\lambda x)$ (resp. the Tchebyshev–Galerkin code) are used for the calculations. Correspondingly the adjoint linear modes are defined by

$$\mathrm{i}\omega(\alpha)\,\mathrm{D}^\dagger \cdot U_1(\alpha) = \mathrm{L}^\dagger_{R(\alpha)} \cdot U_1(\alpha) \tag{A 2}$$

together with the normalization condition

$$\forall \alpha, \alpha', \quad \langle U_1(\alpha),\, \mathrm{D}\cdot V_1(\alpha')\rangle = \delta(\alpha - \alpha'). \tag{A 3}$$

REFERENCES

Abdulrahman, A., Jones, C. A., Proctor, M. R. E. & Julien, K. 2000 Large wavenumber convection in the rotating annulus. *Geophys. Astrophys. Fluid Dyn.* **93**, 227–252.

Azouni, A., Bolton, E. W. & Busse, F. H. 1986 Convection driven by centrifugal buoyancy in a rotating annulus. *Geophys. Astrophys. Fluid Dyn.* **34**, 301–317.

Brummell, N. H. & Hart, J. E. 1993 High Rayleigh number β-convection. *Geophys. Astrophys. Fluid Dyn.* **68**, 85–114.

Busse, F. H. 1970 Thermal instabilities in rapidly rotating systems. *J. Fluid Mech.* **44**, 441–460.

Busse, F. H. & Hood, L. L. 1982 Differential rotation driven by convection in a rapidly rotating annulus. *Geophys. Astrophys. Fluid Dyn.* **21**, 59–74.

Busse, F. H. & Or, A. C. 1986 Convection in a rotating cylindrical annulus: thermal Rossby waves. *J. Fluid Mech.* **166**, 173–187 (referred to herein as BO86).

Clever, R. M. & Busse, F. H. 1989 Nonlinear oscillatory convection in the presence of a vertical magnetic field. *J. Fluid Mech.* **201**, 507–523.

Clune, T. & Knobloch, E. 1993 Pattern selection in rotating convection with experimental boundary conditions. *Phys. Rev.* E **47**, 2536–2550.

Dangelmayr, G. & Kramer, L. 1998 Mathematical Tools for Pattern Formation. In *Evolution of Spontaneous Structures in Dissipative Continuous Systems* (ed. F. H. Busse & S. C. Müller). Lecture Notes in Physics, vol. 55, pp. 1–85. Springer.

Elmer, F. J. 1988 Nonlinear and nonlocal dynamics of spatially extended systems: stationary states, bifurcations and stability. *Physica* D **30**, 321–342.

Greenspan, H. P. 1968 *The Theory of Rotating Fluids.* Cambridge University Press.

Hall, P. 1984 Evolution equations for Taylor vortices in the small-gap limit. *Phys. Rev.* A **29**, 2921–2923.

Hecke, M. V. & Saarloos, W. V. 1997 Convection in rotating annuli: Ginzburg-Landau equation with tunable coefficients. *Phys. Rev.* E **55**, R1259–1262.

Herrmann, J. & Busse, F. H. 1997 Convection in a rotating cylindrical annulus, Part 4: Modulations and transition to chaos at low Prandtl numbers. *J. Fluid Mech.* **350**, 209–229 (referred to herein as HB97).

Jaletzky, M. 1999 Experimental study of rotating cylindrical annulus convection. PhD thesis, University of Bayreuth.

Kuo, E. Y. & Cross, M. C. 1993 Traveling-wave wall states in rotating Rayleigh-Bénard convection. *Phys. Rev.* E **47**, R2245–2548.

Liu, Y. & Ecke, R. E. 1997 Eckhaus-Benjamin-Feir instability in rotating convection. *Phys. Rev. Lett.* **78**, 4391–4394.

Newell, A. C. 1974 Envelope equations. *Lect. Appl. Maths.* **15**, 157–163.

Pierce, R. D. & Knobloch, E. 1994 On the modulational stability of traveling and standing water waves. *Phys. Fluids* **6**, 1177–1190.

Pino, D., Mercader, I. & Net, M. 2000 Thermal and inertial modes of convection in a rapidly rotating annulus. *Phys. Rev.* E **61**, 1507–1517.

Schnaubelt, M. & Busse, F. H. 1992 Convection in a rotating cylindrical annulus, Part 3: Vacillating and spatially modulated flows. *J. Fluid Mech.* **245**, 155–173.

Zhang, K. & Jones, C. A. 1993 The influence of Ekman boundary layers on rotating convection. *Geophys. Astrophys. Fluid Dyn.* **71**, 145–162.

Zhang, K. & Roberts, P. H. 1998 A note on stabilising and destabilising effects of Ekman boundary layers. *Geophys. Astrophys. Fluid Dyn.* **88**, 215–223.